26

RAINFALL ESTIMATION USING A CLOUD PATCH CLASSIFICATION MAP

Kuo-Lin Hsu, Yang Hong, and Soroosh Sorooshian
Department of Civil and Environmental Engineering, University of California, Irvine, CA, USA

1 INTRODUCTION

The development of meteorological satellite systems has been innovating precipitation observations beyond traditional means and enabling frequent observation of precipitation distribution over the remote territories and the broad oceanic regions. In recent years, satellite rainfall estimates from algorithms using geostationary satellite (GOES) sensors and combined GOES and Polar Operational Environmental Satellites (POES) have been rapidly evolving to a certain degree that are suitable as a supplement of the ground in situ observations in providing precipitation information in the hydrological applications. Many precipitation algorithms developed using GOES satellites capable of providing high spatial (4 km) and temporal (15 min) resolution images are considered a unique source for the observation short-term extreme precipitation event (Scofield and Kuligowski 2002).

Although the GOES images are frequently used to measure cloud motion at high resolution, the long-wave infrared image does not provide sufficient information to infer the actual rainfall at the ground surface. Experiments show that the corresponding pixel infrared cloud top brightness temperature and surface rainfall rate is not unique. Therefore, from the local pixel based mapping, a fixed temperature and rainfall rate (T_b-R) function is not capable of fitting surface rainfall rates well at all times. To improve the quality of estimates, strategies have been developed using multiple GOES channels, and adjustment or merging rainfall estimates from multiples sources (Adler et al. 1994; Ba and Gruber 2001; Bellerby et al. 2000; Fulton et al. 1998; Hsu et al. 1997; 1999; Huffman et al. 1997; Huffman et al. 2001; Levizzani et al. 2002; Scofield 1987; Sorooshian et al. 2000; Tapiador et al. 2002; Turk et al. 1998; Vicente et al. 1998; Xie and Arkin 1997; Xu et al. 1999).

V. Levizzani et al. (eds.), Measuring Precipitation from Space: EURAINSAT and the Future, 329–342.

The cloud-top temperature and rainfall relationship is varied with respect to the cloud types and their environmental conditions. Patch-based approaches view the patch coverage as a unit; precipitation under the patch coverage is assigned based on the cloud types, where heavy rainfalls are assigned to the convective active regions and lighter or no rain is assigned to stratiform and cirrus cloud regions. Figure 1 shows the evolution stage of a convective storm. Higher rainfall intensities are usually found during the towering to mature stages, while lower or no-rain appears during the dissipating stage. From the towering stage to the mature stages, cloud top's pixel temperatures near the convective core grew colder, while rainfalls intensified. In the dissipating stage, on the other hand, cloud top temperatures were cold, but had very mild or no corresponding rain.

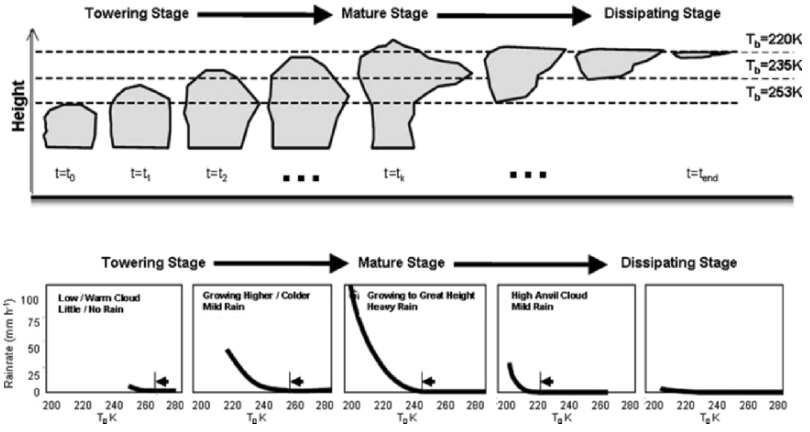

Figure 1. Evolution stages of a convective storm and its rainfall distribution curves.

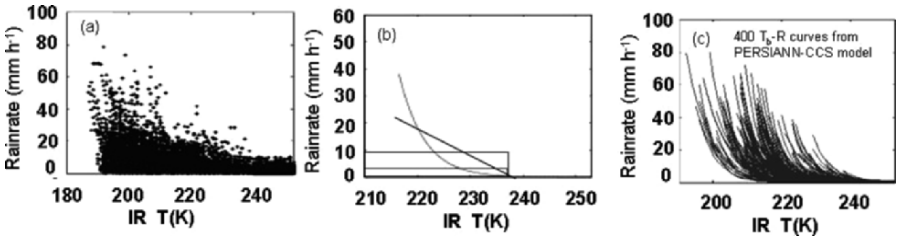

Figure 2. Single fitting curve models vs. a multiple fitting curve model.

Figure 2a shows the scatterplot of T_b-R relationship from a set of GOES image and radar rainfall. The data points are widely spread, which cannot be fitted by a single function (see Fig. 2b). We propose a cloud patch-based rainfall allocation. Cloud patch is assigned a specific T_b-R curve according

to their coldness, size, and texture features. Figure 2c shows 400 T_b-R curves are assigned to the fitting of the scatter points in Fig. 2a.

In this study, a patch-based cloud classification and rainfall estimation algorithm is introduced. This algorithm processes raw satellite image data into the pixel rainfall by series of stages. Details of the algorithm development are described in the following sections.

2 CLOUD PATCH CLASSIFICATION AND RAINFALL ESTIMATION

Humans analyze the world surrounding them by observing and interpreting the patterns that occur in time sequence. Through the distinct features of the patterns shown, knowledge is extracted by classification information into a number of categories and subcategories. In the naming of the cloud system, for example, we classify cloud types as convective and stratus clouds based on their visual appearance in the atmosphere. Convective clouds are puffy and vertically piled up, whereas the stratus are flat and layered, sometimes in fibrous forms. Fine classification of cloud systems is mainly based on the cloud system in different altitude levels, as cumulus, altocumulus, and cumulonimbus for the convective clouds, and stratocumulus, altostratus, cirrostratus, and cirrus for the stratus clouds.

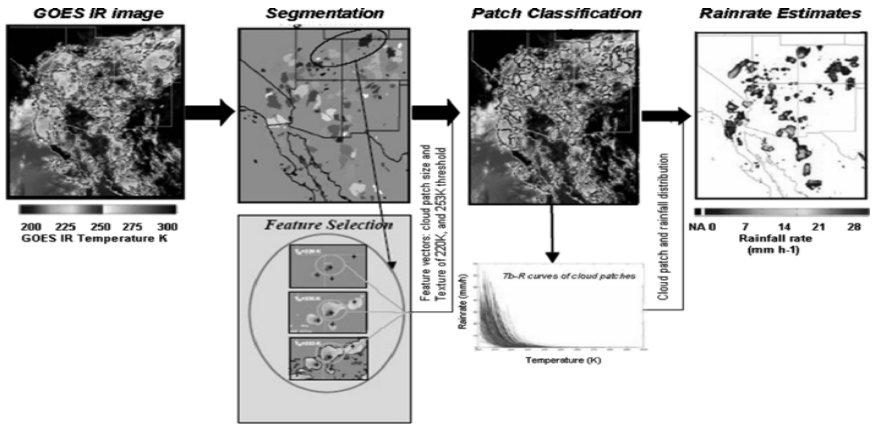

Figure 3. A cloud patch classification and rainfall estimation system.

Observation of the mechanisms of the cloud systems suggests that different types of clouds contain different kinds of thermal ascending and cooling structures and form various distributions of water content. Layer clouds have relatively uniform distribution of water content, while convective clouds have highly variable distribution of water content. Based on their thermal structure, water contents and distribution, different clouds types give diversified precipitation distributions over the ground surface. Although cloud systems

are different in nature, such as high and low, layer or convective clouds, they are discernible with the human eye. However, the implementation of an automatic procedure to detect the cloud types and their associated precipitation from a computer model is not an easy task. It requires great effort to process a huge amount of satellite cloud images and build a cloud patch pattern recognition system which eventually can be used as a tool in providing estimation of precipitation amount and distribution of a rain cloud.

Using computer image processing and pattern recognition techniques, we developed a patch-based cloud classification and rainfall estimation system based on the satellite infrared images. Illustration of the classification system is depicted in Fig. 3 and further descriptions of each stage are as follows.

2.1 Cloud patch segmentation

Segmentation of image data is an important problem for the computer vision, remote sensing, and image analysis. It can be considered a preprocess step before description and recognition of objects. Cloud segmentation is operated through a process that may eventually divide the image into separable patches which are strongly related with cloud systems of the real world contained in the image.

A simple approach to separate patch objects from the background image is by applying a constant brightness threshold. The approach separates the gray image into two levels, high and low. It is simple and makes computation easy. Although a single threshold, 253 K for example, seems to work well in the separation of cloud patch from clear sky or no-precipitating regions, within the patch coverage, it still contains several cloud systems existing at different altitudes with various thermal structures and sizes. Without further separation of those cloud systems from a warm threshold, those distinctive cloud systems are mixed together. As a result the precipitation distribution inside the cloud patch cannot be estimated accurately.

For a better separation of local cloud systems, a watershed-based (topography) segmentation approach is proposed (Vincent and Soille 1991; Dobrin et al. 1994). The algorithm starts from finding the altitude local minima (Fig. 4a), and then follows to fill the basins from the bottom (see Fig. 4b). The water continues to fill all basins. When two basins would merge from the rising the water level, a reservoir is set to separate them (Fig. 4c). While water level continues to rise, individual basins are formed. The process stops when a designed water table is reached (Fig. 4d).

Figure 5 shows the cloud image segmentation using a constant (253 K) threshold and watershed-based separation by gradually increasing threshold temperature from 210 K to 253 K. The source infrared image is listed in Fig. 5a. The constant threshold T_{253K} used to separate pixels under the cloud coverage is listed in Fig. 5b. It shows that several cloud systems are presented in the patch (see Fig. 5a), but a single threshold is not capable of dividing them

into separated patch objects. By applying watershed-based segmentation (Fig. 5c–f), "basins" are filled and separated gradually. Eventually five cloud patches under the threshold temperature of 253 K are identified (see Fig. 5f).

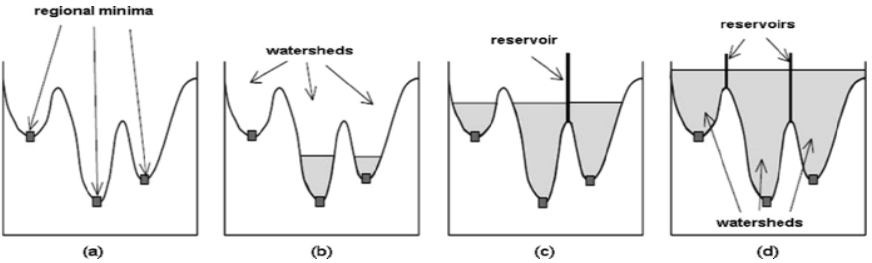

Figure 4. Watershed-based segmentation approach.

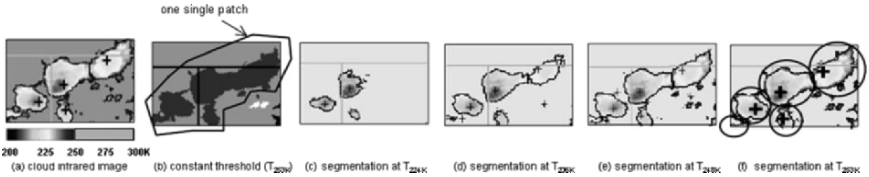

Figure 5. Cloud image separation using watershed-based segmentation approach.

2.2 Patch feature extraction

After the cloud image is separated into a number of objects (patches), it is required to represent the object scenes with a series of attributes or features. Features that are related to the status of cloud patches in the atmosphere, such as the cloud height (lowest temperature), cloud size and shape, surface textures, surface gradients are extracted for the later patch classification. Basically, those selected patch features are separated into three categories: coldness, geometry, and texture (see Table 1). In addition, all the features listed in Table 1 are extracted from three temperature threshold levels (220 K, 235 K, 253 K).

Convective clouds, for example, tend to show puffy and piled up features, whereas stratiform clouds are flat and layered and sometime fibrous in their appearance. Cloud patch features extracted from three separated temperature levels, at 220 K, 235 K, and 253 K demonstrate the existence of the cloud patches at different altitudes in the atmosphere. Figure 6 shows two sets of patch features as extracted from two adjacent cloud patches, denoted as index j and k. After image segmentation, clouds are separated into distinguishable patches. The convective cloud patch j is the mature stage with extensive vertical growth and overshooting top, while convective cloud patch k is in the towering stage, where cloud top brightness temperature is higher than 220 K and therefore the feature vectors at $\bar{V}_{220K}$ are not available (void). Those three

temperature thresholds give a broad classification of cloud patches existing in different altitudes. In addition to the size and texture features, fine classification of cloud patch status and their association with the precipitation amount and distribution in the patch coverage may be investigated.

Table 1. Input features extracted from cloud patches.

Coldness Features of Cloud Patch
1. Minimum temperature of a cloud patch (T_{min})
2. Mean temperature of a cloud Patch (T_{mean})
Geometric Features
3. Cloud patch area (AREA)
4. Cloud Patch Shape Index (SI)
Texture Features
5. Standard deviation of cloud patch temperature (STD)
6. Mean value of local (5×5 pixels) standard deviation of cloud temperature ($MSTD_{5x5}$)
7. Standard deviation of local (5×5 pixels) standard deviation of cloud patch ($STD_{STD:5x5}$)
8. Gradient of cloud cold top brightness temperature (TOPG)
9. Gray image texture (Maximum Angular Second Moment)

2.3 Cloud patch classification

Classification includes concepts such as categorization, identification, recognition, clustering, and partitioning. Supervised and unsupervised learning techniques are often addressed for this purpose. In this study, we use an unsupervised clustering analysis to classify patch samples into a number of cloud patch groups. Clustering is proceeded based on the similarities of patches measured in the their feature space.

The Self-Organizing Feature Map (SOFM) clustering algorithm is used for this purpose (see Fig. 7) (Kohonen 1995; Hsu et al. 1999). The output layer of SOFM is a two-dimensional array of units (or clusters/groups), which are connected to their neighbor units and to the input features. A set of adjustable parameters, called weights, is assigned to the connections between the input features and output units. By sequentially assigning training patterns, the connection weights are adjusted and finally stabilized, i.e., the responses of the output units become ordered. As a result, the similar input features are assigned to the same output unit.

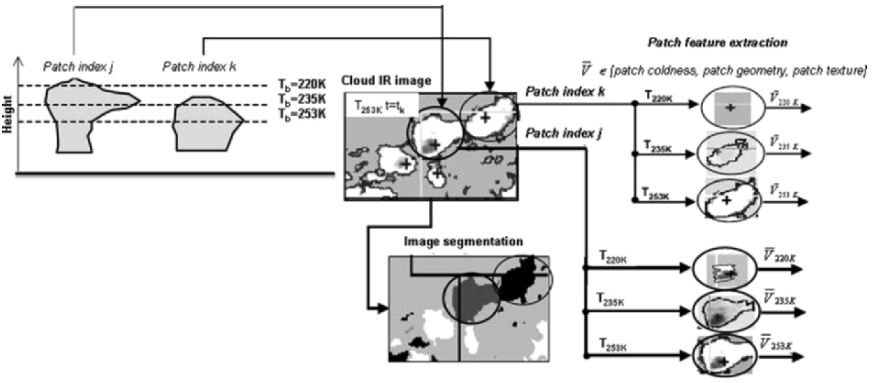

Figure 6. Cloud Patch Feature extraction.

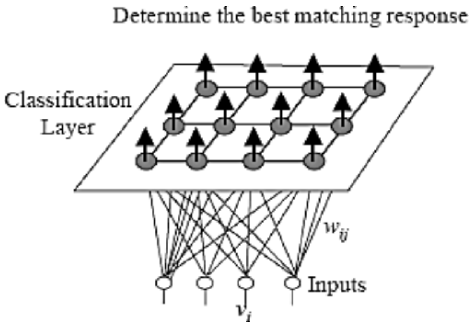

Figure 7. Classification using Self-Organizing Feature Map.

A brief description of the training procedure is summarized below; a detailed description of the training procedure can be found in Kohonen (1995) and Hydkin (1994):

1. Assign random numbers to the weights w_{ij}, where *i* is the index of input feature and *j* is the index of output units.
2. Collect a set of cloud patch samples and normalized as: $\vec{V}(p) = [\vec{V}_{220K}(p), \vec{V}_{235K}(p), \vec{V}_{253K}(p)]$, *p=1...N*, where *N* is the number of training samples.
3. Select a normalized patch sample $\vec{V}(m), m \in [1, N]$ and determine the output unit that has minimized distance between input and connection weights:

$$j^* = \arg\min_j \left\| w_j - \vec{V}(m) \right\| \tag{1}$$

4. For all the units c_j within a neighborhood of radius r of c_j^*, perform the weight update with step size (learning rate) $\alpha > 0$:

$$w_{ij} = w_{ij} + \alpha (v_i (m) - w_{ij}) \tag{2}$$

5. Terminate if the w_{ij} is converged, or reduce r and α, and go to step 3.

2.4 Patch rainfall estimation

Up to the current stage, only a satellite cloud image is required in the image segmentation and cloud patch classification. The next stage is to fit a specific rainfall distribution to each classified cloud patch group. To assign rainfall in the classified patch group, ground radar and low-orbit satellites microwave observations are likely to provide precipitation measurements. For the reliable representation of the classified cloud patch groups and their associated rainfall statistics, samples need to be collected across different seasons and geolocations.

After the patch classification is completed through SOFM training. Assume that a given cloud patch sample is assigned to patch group, c_j, in the SOFM layer. The concurrent cloud temperatures and precipitation pixels under the cloud patch coverage are sampled out and assigned to the patch group c_j. Allocation of pixel rainfall and temperature to the patch groups continues until all the patch samples and rainfall observations are processed. With a sufficient number of samples allocated, a large amount of pixel rainfalls and temperatures are assigned to each of the patch groups in the SOFM layer. The next step was to assign the GOES long-wave infrared temperature (T_b) and hourly radar rainfall rate (R) relationship in each classified patch group.

The Probability Matching Method (PMM) (Atlas et al. 1990) was used to match the relationship between the GOES long-wave infrared temperature and hourly radar rainfall rate. A rainfall probability density function (PDF) is calculated for each patch group in the SOFM layer based on the collected T_b and R samples. It is assumed that lower T_b pixels are associated with higher rain rates. With rainfall rates and infrared brightness temperatures consists of a same accumulated probability matched below:

$$1 - F(T_b^*) = \int_{T_b^*}^{\infty} f(T_b) dT_b = \int_0^{R^*} f(R) dR = F(R^*) \tag{3}$$

where $f(T_b)$ and $f(R)$ are the PDFs of brightness temperature and rainfall rate; whereas $F(T_b^*)$ and $F(R^*)$ are accumulated probability distribution functions of cloud top brightness temperature and radar rainfall, respectively.

In the final step T_b and R data are binned and averaged based on a small temperature increment (ΔT_b) in each patch group. The T_b-R relationship is fitted by a nonlinear function below:

$$R^k = v^k{}_1 + v^k{}_2 \cdot \exp[v^k{}_3 \cdot (T_b + v^k{}_4)^{v^k{}_5}] \tag{4}$$

where R is the rainfall rate (mm h^{-1}), T_b is the cloud top brightness temperature (K), and v^k_1, v^k_2, v^k_3, v^k_4, *and* v^k_5 are parameters with respect to patch group k of SOFM layer parameters [v^k_1, v^k_2, v^k_3, v^k_4, v^k_5] are found from an optimization scheme (Duan et al. 1992).

3 EXPERIMENTS

One month (June 1999) of GOES and stage IV radar data (NCEP) covering the continental USA were collected and processed to the pixel resolution of $0.04^o \times 0.04^o$ latitude/longitude scale. The size of the classification groups was a set of 20 × 20 output units in the SOFM layer (see Fig. 8a). The rational for the selection of the classification group size is that the higher the number of units is assigned to the SOFM layer, the finer the classification of cloud patch samples may be obtained.

The input feature map presents the contour map of the SOFM weight matrix, w_{Ij}. After SOFM is trained, w_{Ij} is the sample mean of an input feature I assigned to the cluster j. Here only three features are listed (see Fig. 8b–d). They show the mean sample value of input patch feature (T_{min}, $AREA_{235K}$, and $MSTD_{5x5\ at\ 235K}$) for the 20 × 20 classification units in the SOFM layer.

It is worth noting the clustering process has organized the T_{min} (see Fig. 8b) in a manner that the higher temperatures appear in the upper region of the map around 220 K to 240 K from the left to the right hand side, while the lower temperatures appear in the lower region of the map range from 220 K to 200 K, from left-to-right locations. This means a patch sample with T_{min} > 230 K will be assigned to the group near the upper-right-hand corner of the SOFM layer. Likewise, a patch sample with T_{min} < 210 K will be assigned to the lower-right-hand corner of the SOFM layer. The average pixel rain rate map (see Fig. 8f) also visually shows its relevance to the T_{min} feature. In general the rain rate map follows the T_{min} feature map, where the lower-half SOFM units appear to contain higher average pixel rain rate.

The $AREA_{235K}$ feature is the patch size below the 235 K threshold. The circled regions of Fig. 8c are associated with large cloud patches. The corresponding patch rainfall volume (see Fig. 8e) is relatively higher in those circled spots, especially on the one where T_{min} is lower than 205 K.

Figure 8d shows the feature map of the average of local standard deviation of 5 × 5 pixels at 235 K-threshold ($MSTD_{5x5\ at\ 235K}$). This feature map represents texture variation in a cloud patch. The circled regions are denoted with higher values of $MSTD_{5x5\ at\ 235K}$, which apparently consist of highly average pixel rain rate (see Fig. 8f). In addition, those high $MSTD_{5x5\ at\ 235K}$ regions are spread from warm to cold cloud patch group (see Fig. 8b).

The calibrated T_b-R curves with respect to the 20 × 20 output units of SOFM layer are listed in Fig. 9. With reference to the T_{min} shown in Fig. 8b, one could identify those T_b-R curves being associated with patch minimum temperature ranged from 240 K to 200 K. Accompanying with the input feature maps of $AREA_{235K}$ (Fig. 8c) and $MSTD_{5x5\ at\ 235K}$ (Fig. 8d), we may further explain the T_b-R curves and their relevance to the various cloud top temperatures (T_{min}), patch sizes ($AREA_{235K}$), and patch texture variations ($MSTD_{5x5\ at\ 235K}$).

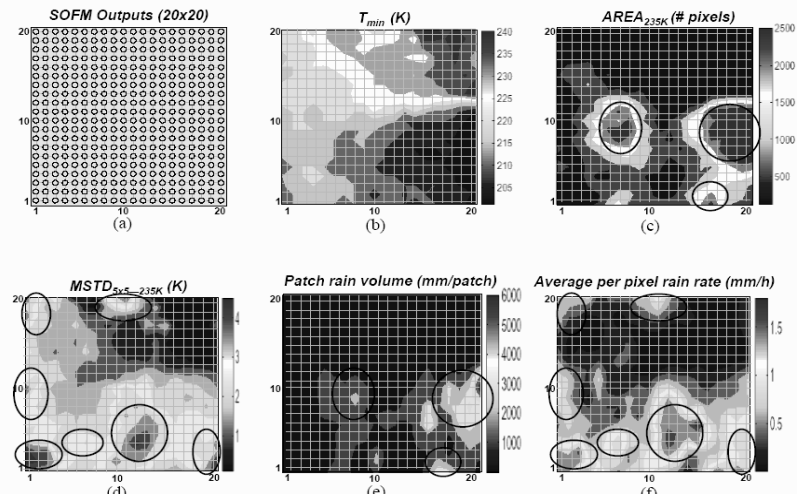

Figure 8. Input feature maps (see also color plate 12).

In Fig. 9b, several regions, denoted as G_0-G_6, containing special T_b-R curve groups, are located. Cloud groups on G_0 are no-rain warm cloud; cloud groups on G_1 and G_2 are around the same T_b range, but associated with two different slopes of T_b-R curves. Both G_1 and G_2 contain T_{min} around 230 K and higher, however, a cloud patch classified in G_1 region has a lower $MSTD_{5x5\ at\ 235K}$ than G_2 region. Cloud groups on G_3 and G_4 also represent cloud patch groups with T_{min} around 215 K and above. G_4 group has much higher local texture variations

($MSTD_{5x5\ at\ 235K}$) than G_3 group. As a result, the slopes of T_b-R curves are steeper on group G_4. Likewise, the slopes of T_b-R curves are steeper on G_6 region than on G_5 region. Although both regions represent patches T_{min} around 200 K, the $MSTD_{5x5\ at\ 235K}$ map (Fig. 8d) reveals that the higher *MSTD* value, the steeper T_b-R curves.

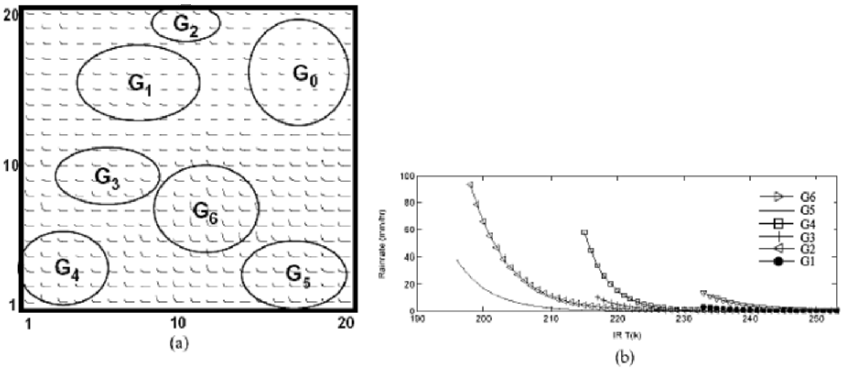

Figure 9. Cloud patch groups (G_0 to G_6) contain special T_b-R curves.

Figure 10 shows the lifetime of a convective cloud system and its T_b-R curves. The time period from 1440 UTC to 1900 UTC is the towering to mature stages of the cloud patch, while after 1900 UTC, the cloud patch is in the recession and decay stage. The cloud T_b distribution in the evolution stage of cloud patch is listed in Fig. 10a, while the corresponding sorted T_b-R distribution is displayed in Fig. 10b (the dot plots are the averaged radar rainfall binned at 1 K T_b interval. The line plots are the fitting curves based on the regression functions). They show that the T_b-R curves progressively varied during the evolution stage of a convective storm. One can imagine that the estimation of rainfall rates may not perform well, if only one fixed T_b-R function is assigned to all of the stages.

Figure 11 shows hourly rainfall estimates over east New Mexico area during a consecutive 6-h time period, from 00UTC to 05UTC of July 4, 2002. Precipitation observation from NCEP stage IV radar estimates is listed in the upper panel, while the rainfall estimates from cloud patch classification system is listed in the lower panel. The image is processed at $0.04^o \times 0.04^o$ latitude/longitude scale. It shows that rainfall regions are well matched from both radar and model's estimates.

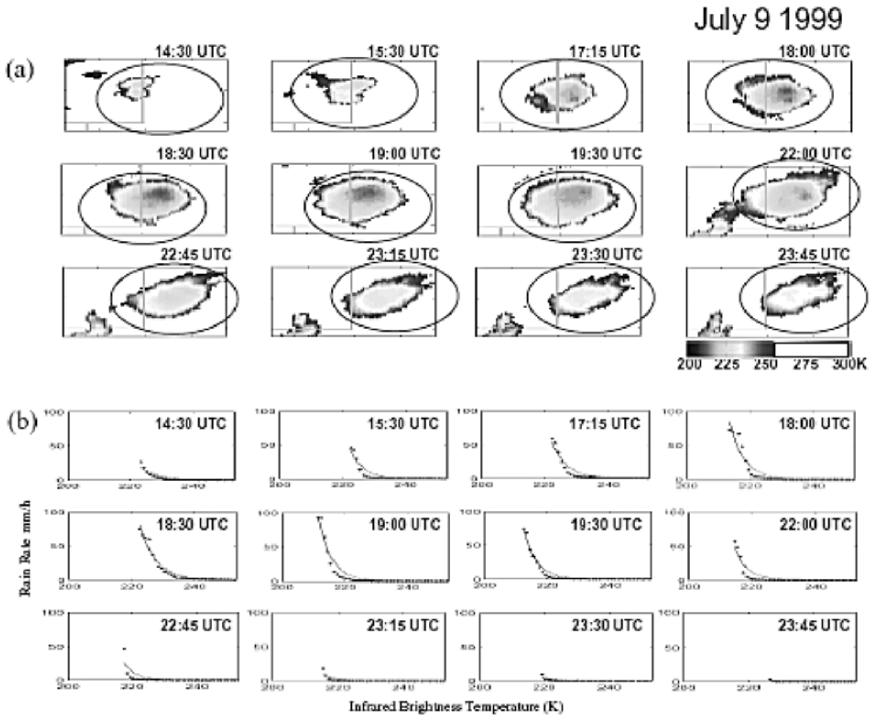

Figure 10. The evolution process of a convective cloud and its Tb-R curves.

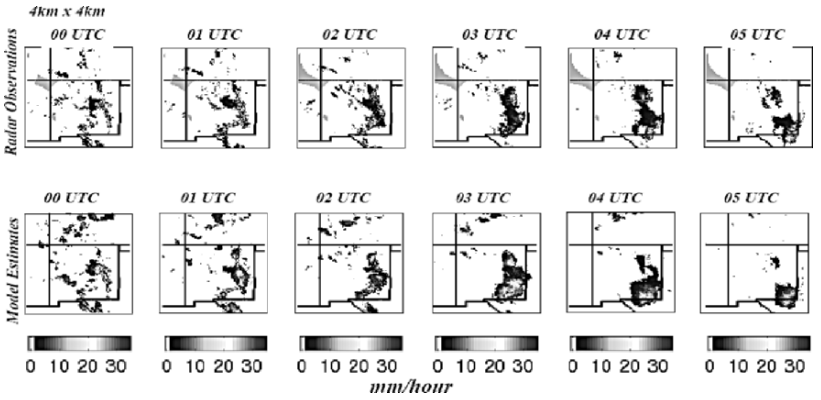

Figure 11. Rainfall estimates during 6-h period.

4 CONCLUSIONS

This paper describes a cloud patch classification approach applied to the surface rainfall estimation. This approach implements image processing and pattern classification techniques to the analysis of long-wave infrared (10.7 μm) cloud images of GOES satellites. In low-level image processing, segmentation using a watershed-based scheme is used to separate cloud patches from their image background. This is followed by image extraction and interpretation where cloud patches are treated as independent objects and are described by object features such as patch coldness, size, shape, and texture. Classification of cloud patch objects is based on an unsupervised clustering scheme. When the patch rainfall is assigned to the classified patch group, the interpretation of the cloud patch property and rainfall relationships are established. Finally, the rainfall distribution of the classified patch group is described by a set of infrared brightness temperature and rainfall rate (T_b-R) functions. Parameters of the nonlinear T_b-R function are calibrated from the spatial and temporal co-located satellite image and radar rainfall map.

Multiple seasons of rainfall estimates were generated and evaluated using ground gauge and radar data. Details of the evaluation performance can be found from Hong et al. (2004). For the potential extension of precipitation estimates over the oceans and remote regions, we are exploring using TRMM satellite rainfall measurements in the calibration of model parameters. Evaluation of those results will be discussed in a separate report.

Acknowledgements: Support for this research was provided by NASA's EOS, TRMM, and HyDIS and NSF STC-SAHRA research programs. Data used in this study is provided from NOAA Climate Prediction Center and National Center for Environmental Prediction. It is a pleasure to acknowledge Dan Braithwaite for his processing the data required for this study and Ms. Diane Hohnbaum for her editing of the manuscript.

5 REFERENCES

Adler, R. F., G. J. Huffman, and P. R. Keehn, 1994: Global rain estimates from microwave adjusted geosynchronous IR data. *Remote Sens. Rev.*, **11**, 125–152.

Atlas, D., D. Rosenfeld, and D. B. Wolff, 1990: Climatologically tuned reflectivity-rainrate relationship and links to area-time integrals. *J. Appl. Meteor.*, **29**, 1120–1135.

Ba, M. B. and A. Gruber, 2001: GOES multiple spectral rainfall algorithm (GMSRA). *J. Appl. Meteor.*, **40**, 1500–1541.

Bellerby, T., M. Todd, D. Kniveton, and C. Kidd, 2000: Rainfall estimation from a combination of TRMM Precipitation Radar and GOES multispectral satellite imagery through the use of an artificial neural network. *J. Appl. Meteor.*, **39**, 2115–2128.

Dobrin, B. P., T. Viero, and M. Gabbouj, 1994: Fast watershed algorithms: analysis and extensions. *Nonlinear Image Processing V.*, **2180**, 209–220.

Duan, Q., S. Sorooshian, and V. K. Gupta, 1992: Effective and efficient global optimization for conceptual rainfall-runoff model. *Water Resource Res.*, **28**(4), 1015–1031.

Fulton, R. A, J. P. Breidenbach, D. J. Seo, and D. A. Miller, 1998: The WSD-88D rainfall algorithm. *Wea. Forecasting,* **13**, 377–395.

Hong, Y., K. Hsu, X. Gao, and S. Sorooshian, 2004: Precipitation estimation from remotely sensed information using an artificial neural network-cloud classification system. *J. Appl. Meteor.*, **43**, 1834–1853.

Hsu, K, X. Gao, S. Sorooshian, and H. V. Gupta, 1997: Precipitation estimation from remotely sensed information using artificial neural networks. *J. Appl. Meteor.*, **36**, 1176–1190.

Hsu, K., H. V. Gupta, X. Gao, and S. Sorooshian, 1999: Estimation of physical variables from multichannel remotely sensed imagery using a neural networks: application to rainfall estimation. *Water Resource Res.*, **35**(5), 1605–1618.

Huffman, G. J., R. F. Adler, P. A. Arkin, A. Chang, R. Ferraro, A. Gruber, J. Janowiak, A. McNab, B. Rudolph, and U. Schneider, 1997: The Global Precipitation Climatology Project (GPCP) combined precipitation dataset. *Bull. Amer. Meteor. Soc.*, **78**, 5–20.

Huffman, G. J., R. F. Adler, M. M. Morrissey, D. T. Bolvin, S. Curtis, R. Joyce, B. McGavock, and J. Susskind, 2001: Global precipitation at one-degree daily resolution from multi-satellite observations. *J. Hydrometeor*., **2**, 36–50.

Hykin, S., 1994: *Neural Networks: A Comprehensive Foundation.* Macmillan College Pub.

Kohonen, T., 1995: *Self-Organizing Map*. Springer-Verlag.

Levizzani, V., J. Schmetz, H. J. Lutz, J. Kerkmann, P. P. Alberoni, and M. Cervino, 2000: Precipitation estimations from geostationay orbit and prospects for METEOSAT Second Generation. *Meteor. Appl.*, **8**, 23–41.

[NCEP] National Center for Environmental Prediction, National Stage IV QPE Product. http://www.emc.ncep.noaa.gov/mmb/ylin/pcpanl/stage4.

Scofield, R. A., 1987: The NESDIS operational convective precipitation technique. *Mon. Wea. Rev.*, **115**, 1773–1792.

Scofield, R. A. and R. J. Kuligowski, 2002: Status and outlook of operational satellite precipitation algorithms for extreme precipitation events. *Proc. 1st Workshop Int. Precipitation Working Group*; September 23–27 2002; Madrid, Spain, 43–51.

Sorooshian, S., K. Hsu, X. Gao, H. V. Gupta, B. Imam, and D. Braithwaite, 2000: An evaluation of PERSIANN system satellite-based estimations of tropical rainfall. *Bull. Amer. Meteor. Soc.*, **81**(9), 2035–2046.

Tapiador, F. J., C. Kidd, V. Levizzani, and F. S. Marzano, 2002: A neural network PMW/IR combined procedure for short term/small area rainfall estimates. *Proc. 1st Workshop Int. Precipitation Working Grou*p, September 23–27 2002, Madrid, Spain, 167–173.

Turk, F. J., F. S. Marzano, and E. A. Smith, 1998: Combining geostationary and SSM/I data for rapid rain rate estimation and accumulation. *Proc. 9th Conference on Satellite Meteorology and Oceanography*, Paris, 462–465.

Vicente, G., and R. A. Scofield, 1998: The operational GOES infrared rainfall estimation technique. *Bull. Amer. Meteor. Soc*., **79**, 1883–1898.

Vincent, L. and P. Soille, 1991: Watersheds in digital spaces: an efficient algorithm based on immersion simulations." *IEEE Trans. Pattern Ana. Machine Intell*., **13**(6), 583–598.

Xie, P. and P. A. Arkin, 1997: Global precipitation: A 17 years observation based on gauge observations, satellite estimates and numerical model outputs. *Bull. Amer. Meteor. Soc.*, **78**, 2539–2558,.

Xu, L., X. Gao, S. Sorooshian, P. A. Arkin, and B. Imam, 1999: A microwave-infrared threshold technique to improve the GOES Precipitation Index. *J. Appl. Meteor.*, **38**, 569–579.

COLOR PLATES

Plate 1. Time longitude sections at 5º N–5º S, January 1997–October 1998; GPCP Version 2 monthly, pentad and daily data. *(Figure 3 of Gruber et al., Section 1)*

Plate 2. Air pollution decreases the drop sizes of convective clouds over the British Isles. This NOAA-AVHRR image from 18 April 1995, 1337 UT was analyzed by the scheme of Rosenfeld and Lensky (1998), showing convective rain clouds with large drops (r_e > 20 μm, well exceeding the 14 μm precipitation threshold) in the northwesterly flow from the Atlantic Ocean. The clouds interact with the air pollution over the populated land areas and become composed of small drops (re < 10 μm, too small for precipitating) that appear in yellow shades. Note that the sharp distinction of the clouds around the latitude of Glasgow. Northern Scotland is sparsely populated and hence the clouds remain pristine with large drops, as indicated by the red shades. *(Figure 3 of Rosenfeld, Section 1)*

Plate 3. MSG image from 20 May 2003 1342 UTC, over central Africa at a 1200 × 1200 km^2 rectangle between 1–12N and 15–26E. The area shows the transition between the relatively microphysically maritime clouds over the forested area (dark surface) and microphysically continental clouds over the dry lands of the Sahel to the north (bright surface). The T-r_e relations of the continental clouds (1) show much smaller r_e for a given T compared to the maritime clouds (2). The median re of the maritime clouds (the yellow line) saturates near T = –20°C, indicating glaciation at that temperature. The small median re at area 1 even above the –40°C isotherm indicates homogeneous glaciation of the cloud water and hence low precipitation efficiency. The color scheme is red for the visible, green for 3.9 μm reflectance component, and blue for temperature. For full description and interpretation of the color table is given in Rosenfeld and Lensky (1998). The T-r_e lines represent percentiles of r_e for a given T in 10% steps for each line, between 5% and 95%. The median is between the yellow and green lines. *(Figure 4 of Rosenfeld, Section 2)*

Plate 4. Sample of the diffusion rainfall estimation method of Tapiador et al. compared with an IR-based procedure and the actual radar data. *(Figure 6 of Tapiador et al., Section 2)*

Plate 5. Mean rainrate (*RR*) in the fore/after T_B plane at 19.3_H GHz (left panels) and 85.5_H GHz (right panels). Top and bottom panels correspond to the simulations of the Goddard Cumulus Ensemble (GCE) *TCOF*22 and *MIDACF*. *(Figure 4 of Battaglia et al., Section 2)*

Plate 6. (a) Retrieved conditional rainfall; (b) probability of rain; (c) retrieved conditional rain for probability of rain greater than 50%; (d) uncertainty of rain [%]. Rain retrieval algorithm of Kummerow et al. *(Figure 7 of Kummerow et al., Section 3)*

Plate 7. 24-h rainfall potential (inches) (*right*) derived from SSM/I instantaneous rain rates (*left*) on 1510 UTC, 18 September 2003 for Hurricane Isabel. *(Figure 1 of Ferraro, Section 3)*

Plate 8. (a) Fraction of precipitation events with snowfall at the surface over the northern Atlantic for October 2002; (b) total number of precipitation events found per 0.5 × 0.5 degree box; (c) same as (a) but for January 2003; (d) same as (b) but for January 2003. *(Figure 4 of Bennartz, Section 3)*

Plate 9. Mean surface rain rates, convective rain proportions, and latent heating rates at 7 and 3 km altitude, derived from TMI observations from January 2000, using the GPROF algorithm. *(Figure 5 of Olson et al., Section 3)*

Plate 10. Final combined HQ+VAR precipitation field computed with the Real-Time MPA for 1500 UTCon 15 September 2004. Zero values are colored white if computed by the HQ and gray if by VAR; all other precipitation values have the same color value for both sources. *(Figure 3 of Huffman et al., Section 4)*

Plate 11. Cumulated rainfall (mm h^{-1}) from the MICRA algorithm on November 1–17, 1999, within the Meteosat sector. *(Figure 2 of Marzano et al., Section 4)*

Plate 12. Input feature maps of the rainfall estimation technique based on cloud patch classification maps of Hsu et al. *(Figure 8 of Hsu et al., Section 4)*

Plate 13. Precipitation (mm day^{-1}) for January 1994 as observed in the satellite estimates of GPI, SSM/I scattering (SCT), SSM/I emission (EMS), OPI, MSU, the gauge-based analysis, the NCEP/NCAR reanalysis (REANAL), and the merged analysis. *(Figure 1 of Xie et al., Section 4)*

Plate 14. 10 November 2001, 0300 UTC; *upper left*: BOLAM model; *upper right*: combined IR-MW NRL Turk algorithm estimate; *bottom*: IR NRE (neural rain estimator) estimate. *(Figure 5 of Kästner, Section 5)*

Plate 15. 12-h accumulated precipitation (mm h^{-1}), 1200 UTC, 10 Nov. 2001 (Algiers flood): estimated from satellite (*upper left*), reference forecast (R, *upper right*), and for the assimilation run (N, *bottom*) of the BOLAM model. *(Figure 5 and 6 of Buzzi and Davolio, Section 6)*

Plate 16. Analysis increments of TCWV (in kg m^{-2}) on April 7, 2003, 0000 UTC from all observations (a) and rain observations (b). (c) 48 h-24 h precipitation forecast (in 10^{-3} mm) initialized on April 1, 2003, 1200 UTC with rain observations. *(Figure 5 of Bauer et al., Section 6)*

Plate 17. 6 August 2002. Rain intensity maps in mm h^{-1} for the Emilia-Romagna storm case study. All times are UTC. (a) Radar map at 0012; (b) NRLT for the slot starting at 0000; (c) Radar map at 0042; (d) NRLT for the slot starting at 0030; (e) NRLT for the slot starting at 0630; (f) PMW NESDIS algorithm for the SSM/I orbit 08D (F13) starting at 0627; (g) NRLT for the slot starting at 0700; (h) Radar map at 0642; (i) NRLT for the slot starting at 0800; (j) PMW NESDIS algorithm for the SSM/I orbit 10D (F14) starting at 0828; (k) NRLT for the slot starting at 0800; (l) Radar map at 0842; (m) NRLT for the slot starting at 0930; (n) PMW NESDIS algorithm for the SSM/I orbit 12D (F15) starting at 0941; (o) NRLT for the slot starting at 1000; (p) Radar map at 0942. *(Figure 1 of Torricella et al., Section 7)*

Plate 18. January 1-10 (decade 1) 2003 rainfall accumulation estimate in mm (*top*), and maize yield projection (% yield potential) based on estimated rainfall and an empirical equation (*bottom*). White spaces denote zero yield potential. *(Figure 7 and 8 of Liu et al., Section 7)*

Plate 19. MM5 and discrete ordinate Jacobian simulations at 424.763 ± 4 GHz of Hurricane Bonnie at landfall (courtesy of A. J. Gasiewski). *(Figure 8 of Bizzarri et al., Section 8)*

Plate 20. (a) CWCs of six hydrometeor species [cloud droplets (*top left*), rain drops (*top middle*), graupel (*top right*), pristine crystals (*bottom left*), snowflakes (*bottom middle*), and aggregates (*bottom right*)] for inner grid of UW-NMS snowstorm simulation at time step 1800 s (i.e., 0600 UTC, 25 January 2000). Vertical lines indicate path of vertical cross-section in Plate 18b.
(b) Synthetic snow IWC retrievals for selected cross-section of eastern U.S. snowstorm simulation. Left panels from top to bottom are: (1) EGPM radiometer retrieval using only four lower window frequencies, i.e. 18.7, 23.8, 36.5 and 89 GHz (similar to four SSM/I frequencies), (2) as previously but using all five window frequencies including 150 GHz, (3) as previously but using all five window frequencies plus four pairs of sounding channels in 50–54 and 118 GHz regions, (4) combined EGPM radar-radiometer retrievals, and for comparison (5) model "truth". For each retrieval case, associated right panels show estimated average profile (blue solid line) together with model "truth" average profile (red line), plus retrieval error standard deviations at various atmospheric levels (blue error bars). *(Figure 3 and 7 of Mugnai et al., Section 8)*

Plate 21. Distributions of monthly rainfall accumulation over global tropics for Feb 1998 produced by most recent version (V6) of standard TRMM L2 / L3 algorithms: (1) top panel shows TMI-only (L2 alg 2a12) (see Kummerow et al. 1996, 2001; Olson et al. 2001, 2007); (2) 2nd from top panel shows PR-only (L2 alg 2a25) (see Iguchi et al. 2000; Meneghini et al. 2000); (3) 3rd from top panel shows TMI-PR Combined (L2 alg 2b31) (see Haddad et al. 1997; Smith et al. 1997); and (4) bottom panel shows TMI-only (L3 alg 3a11) (see Wilheit et al. 1991; Hong et al. 1997; Tesmer and Wilheit 1998). Color bar denotes average rainrate in mm day^{-1}. *(Figure 3 of Smith et al., Section 8)*

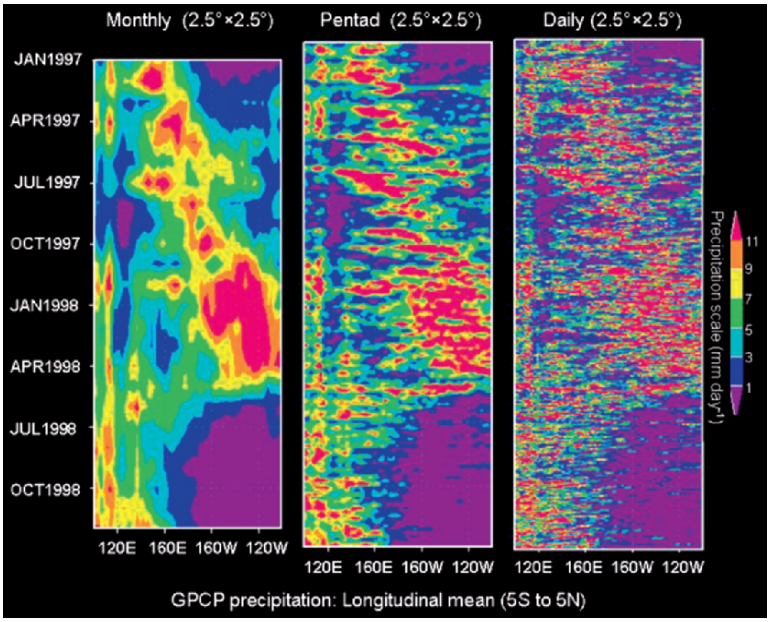

Plate 1

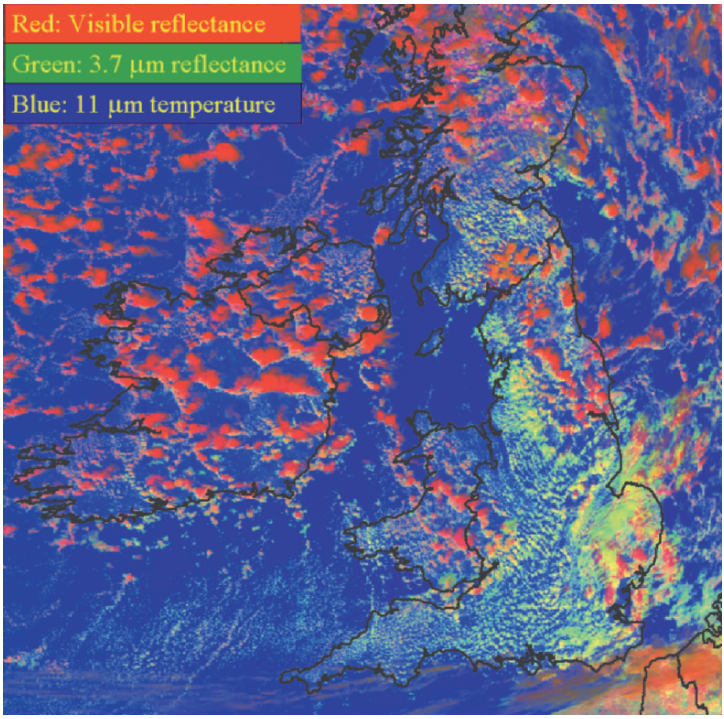

Plate 2

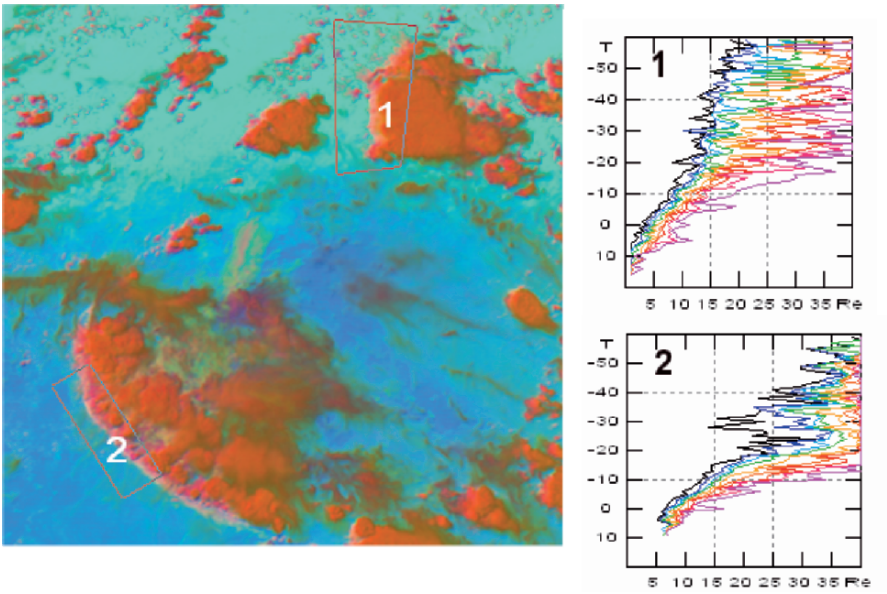

Plate 3

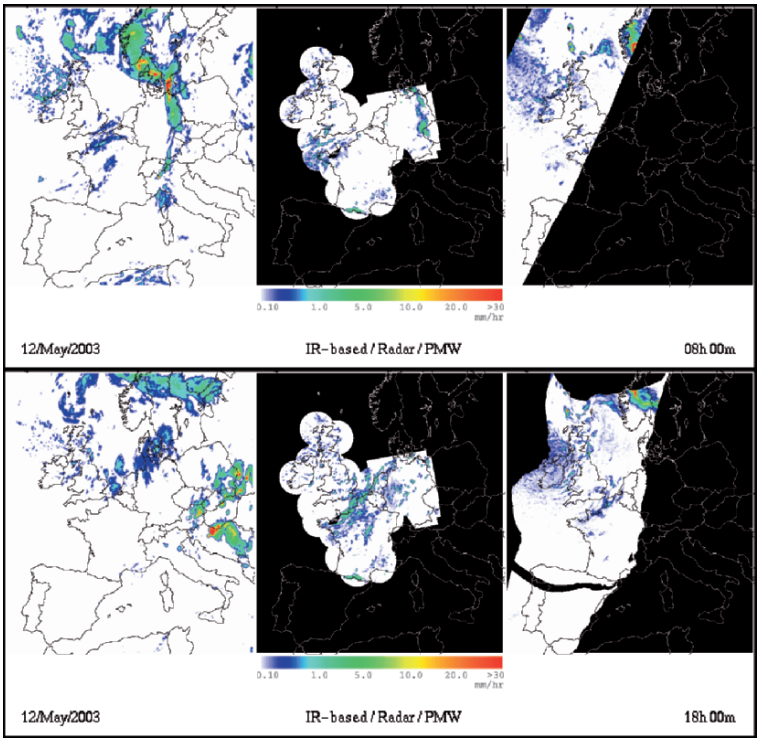

Plate 4

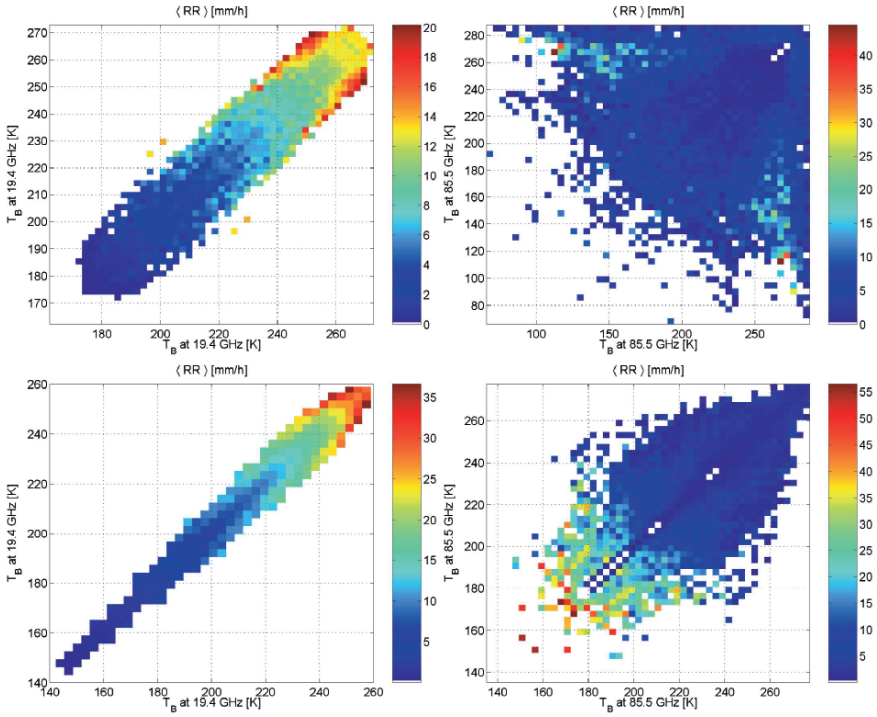

Plate 5

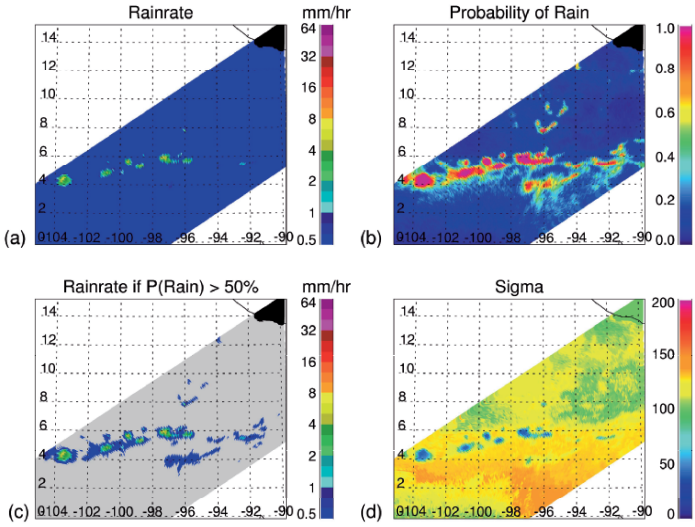

Plate 6

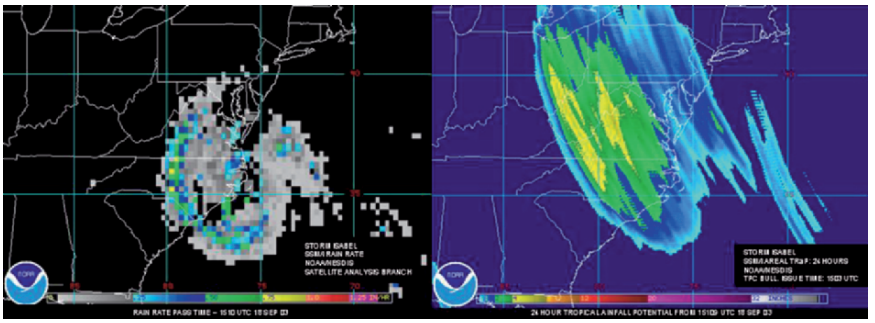

(a) **(b)**

Plate 7

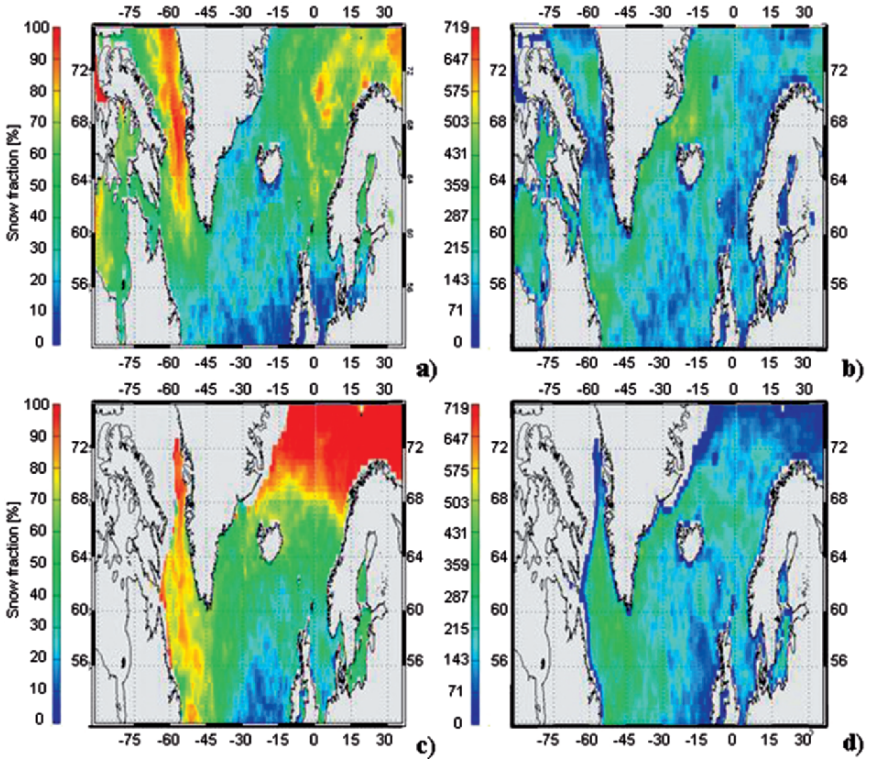

Plate 8

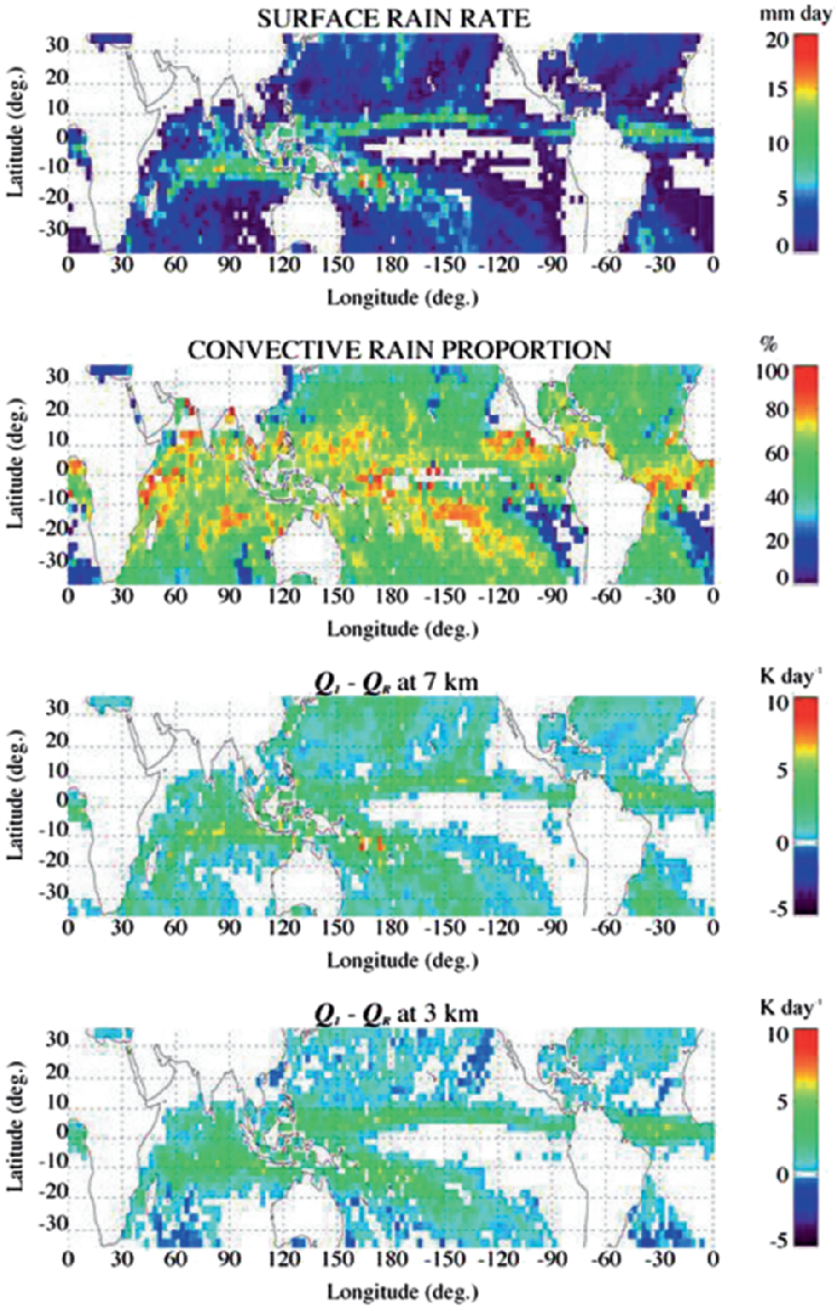
SURFACE RAIN RATE
mm day
20
15
10
5
0
Latitude (deg.)
30
20
10
0
-10
-20
-30
0 30 60 90 120 150 180 -150 -120 -90 -60 -30 0
Longitude (deg.)
CONVECTIVE RAIN PROPORTION
%
100
80
60
40
20
0
Latitude (deg.)
Longitude (deg.)
Q_1 - Q_R at 7 km
K day^{-1}
10
5
0
-5
Latitude (deg.)
Longitude (deg.)
Q_1 - Q_R at 3 km
K day^{-1}
10
5
0
-5
Latitude (deg.)
Longitude (deg.)

Plate 9

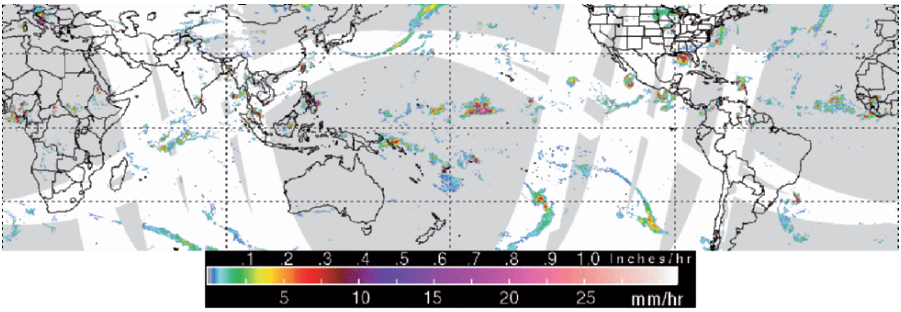

Plate 10

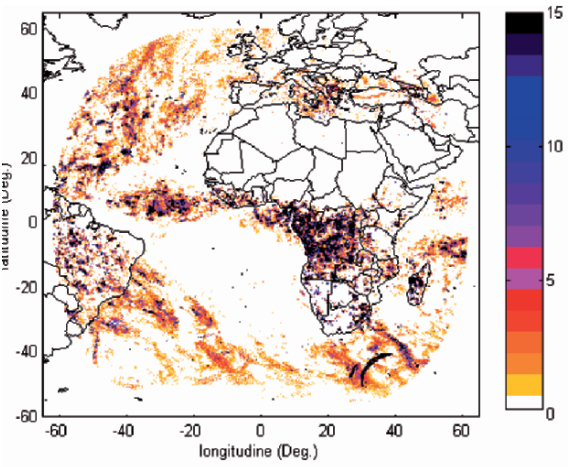

Plate 11

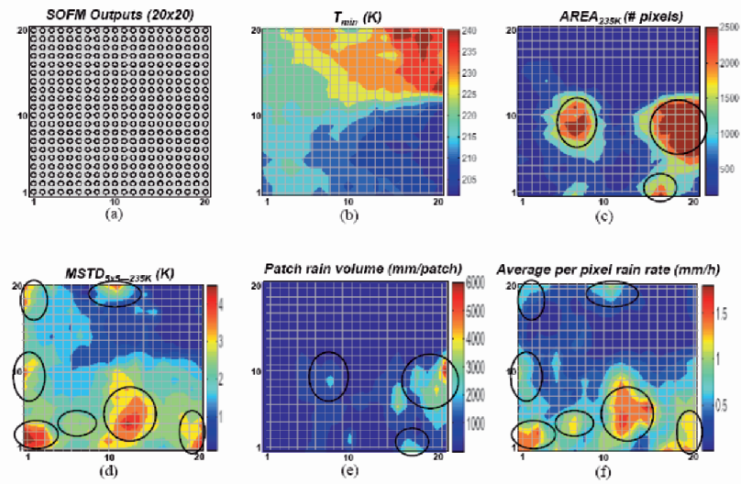

Plate 12

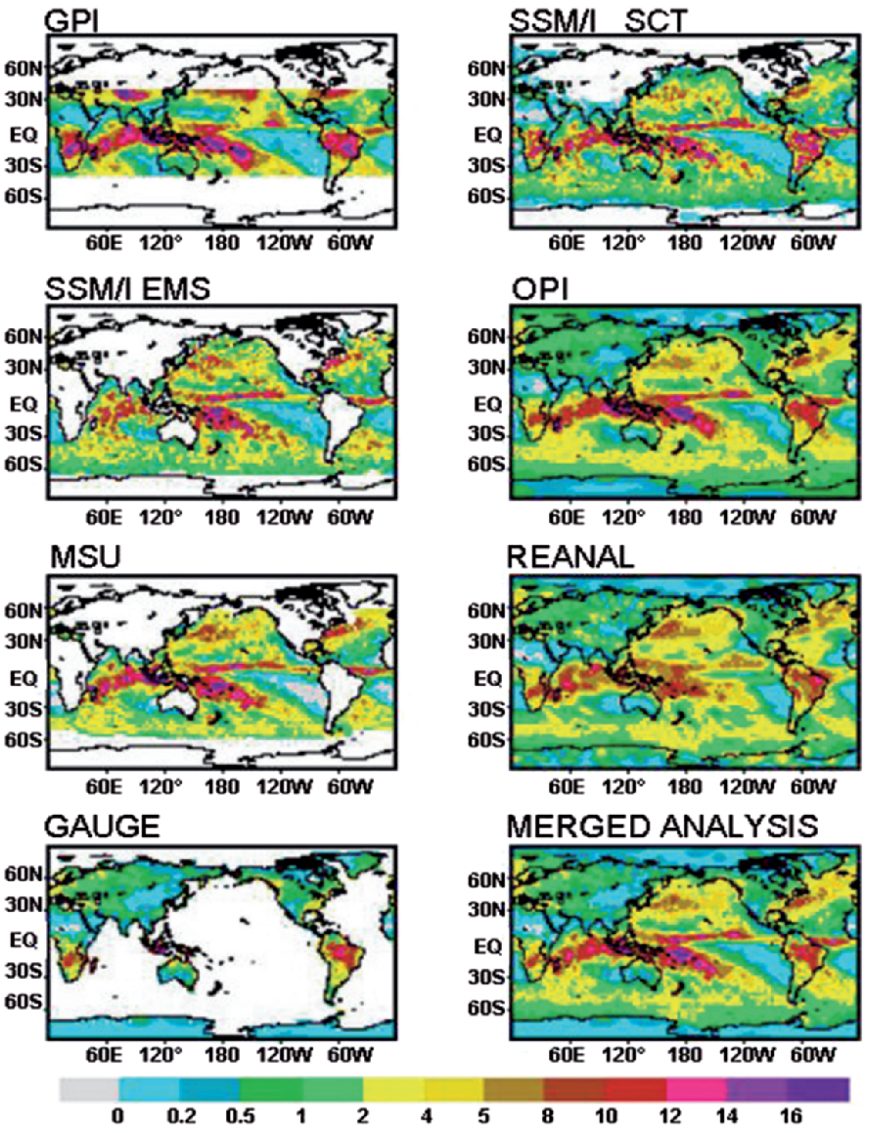
GPI
SSM/I SCT
SSM/I EMS
OPI
MSU
REANAL
GAUGE
MERGED ANALYSIS
60N
30N
EQ
30S
60S
60E 120° 180 120W 60W
0 0.2 0.5 1 2 4 5 8 10 12 14 16

Plate 13

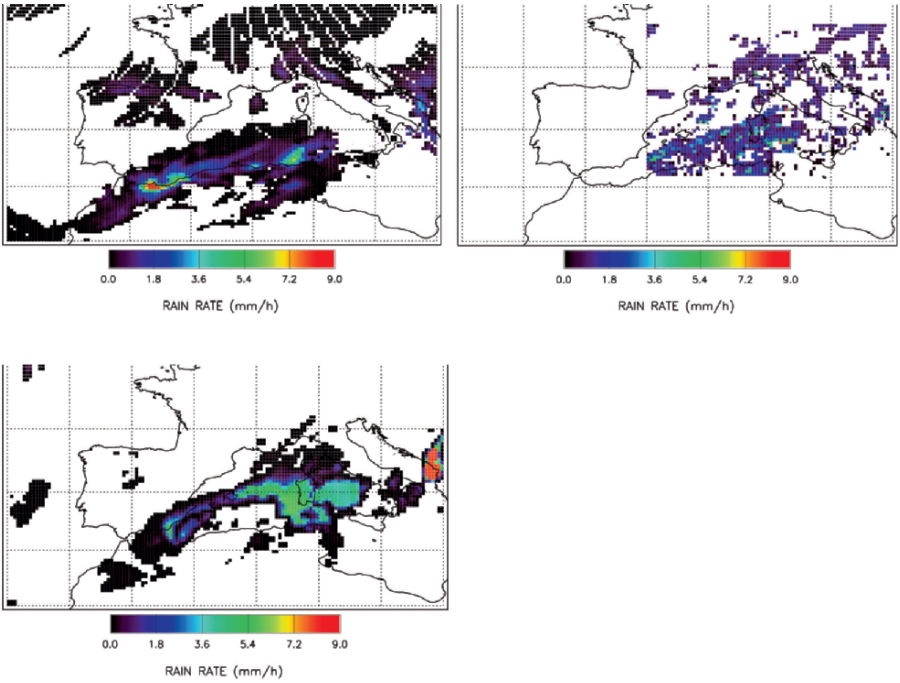

Plate 14

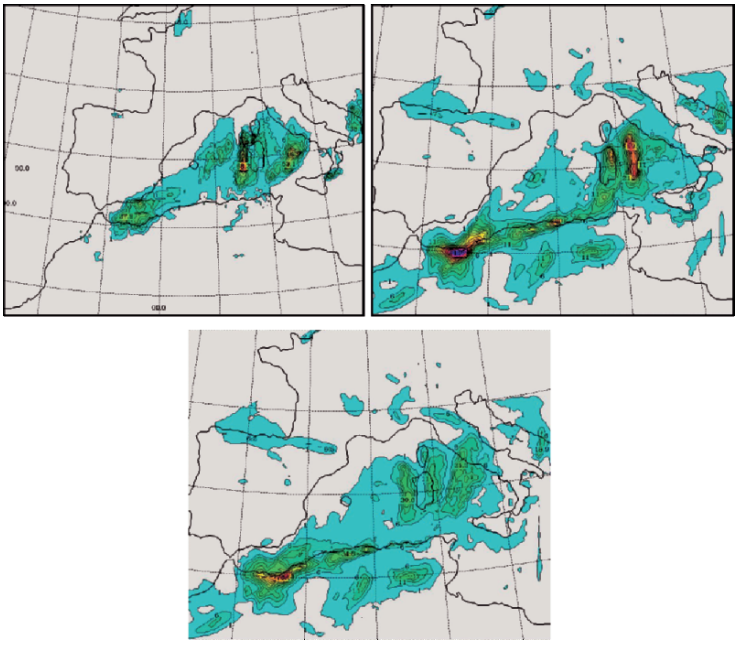

Plate 15

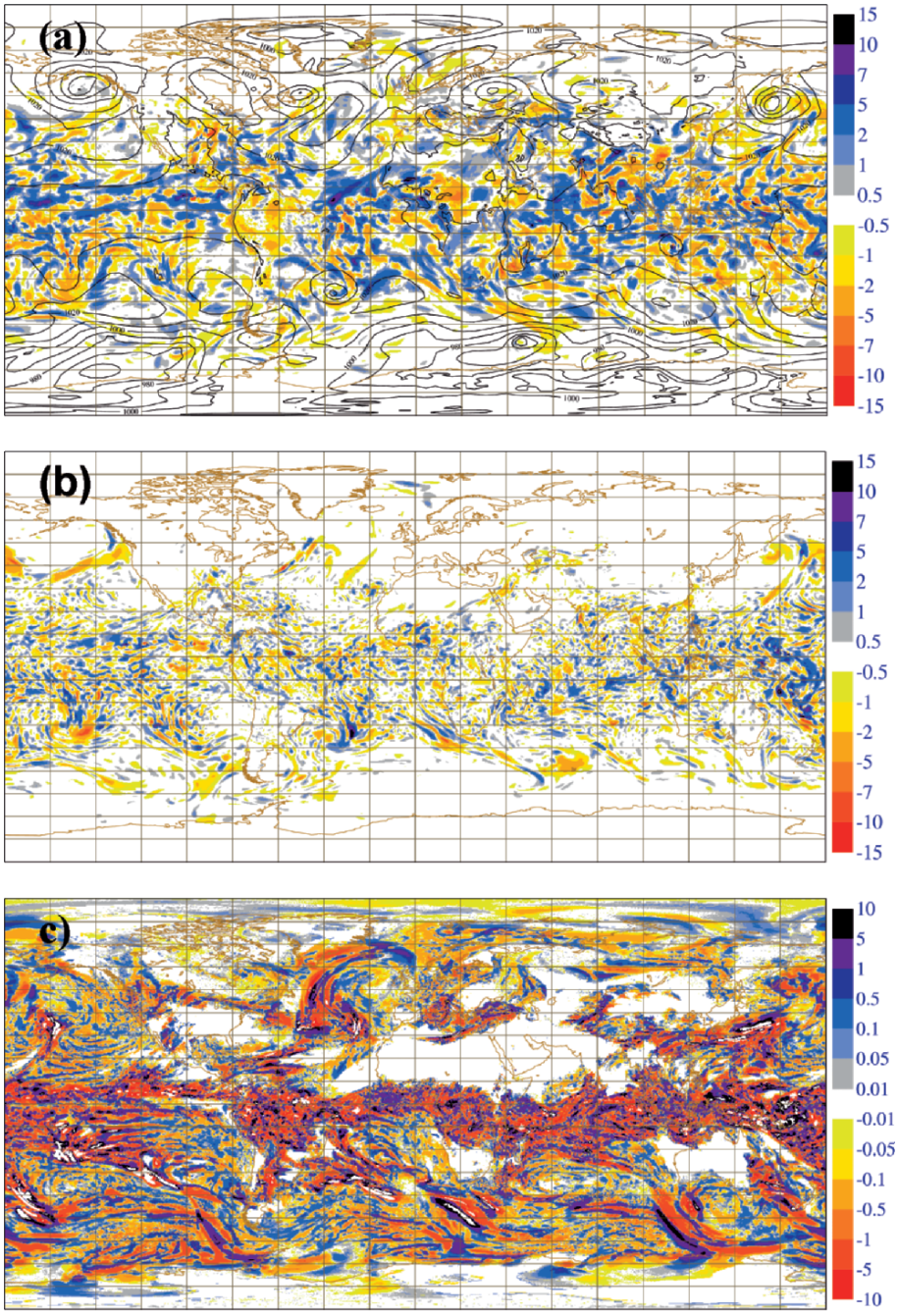
(a)
15
10
7
5
2
1
0.5
-0.5
-1
-2
-5
-7
-10
-15
(b)
15
10
7
5
2
1
0.5
-0.5
-1
-2
-5
-7
-10
-15
(c)
10
5
1
0.5
0.1
0.05
0.01
-0.01
-0.05
-0.1
-0.5
-1
-5
-10

Plate 16

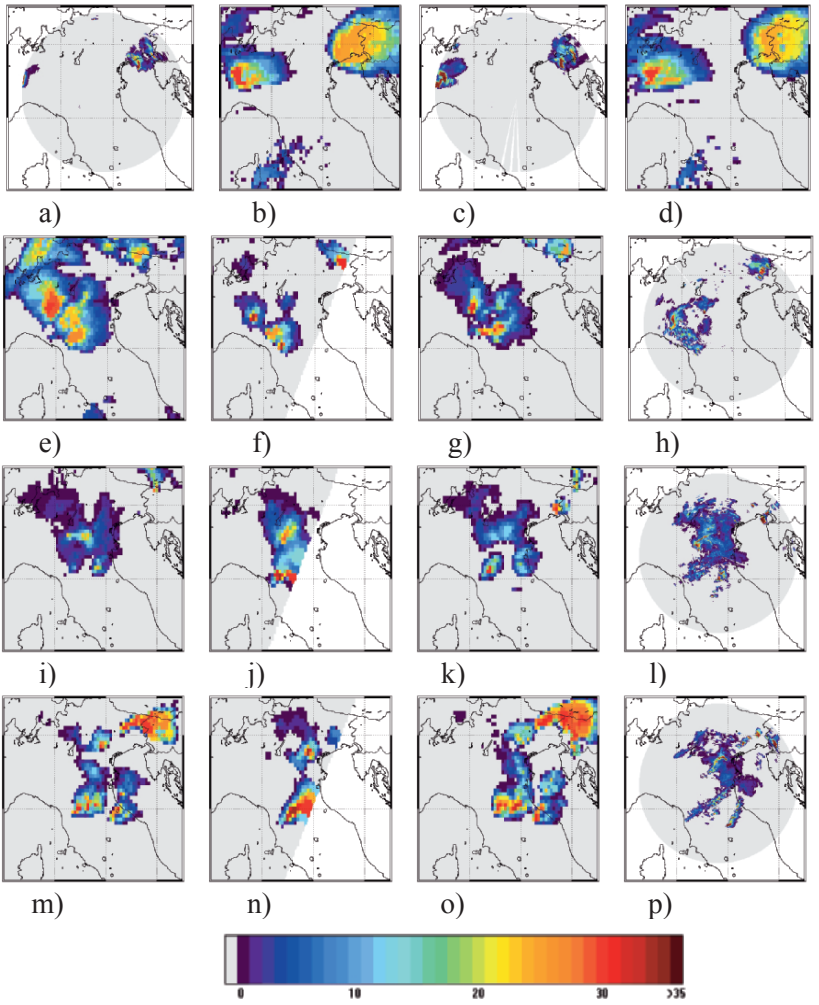

Plate 17

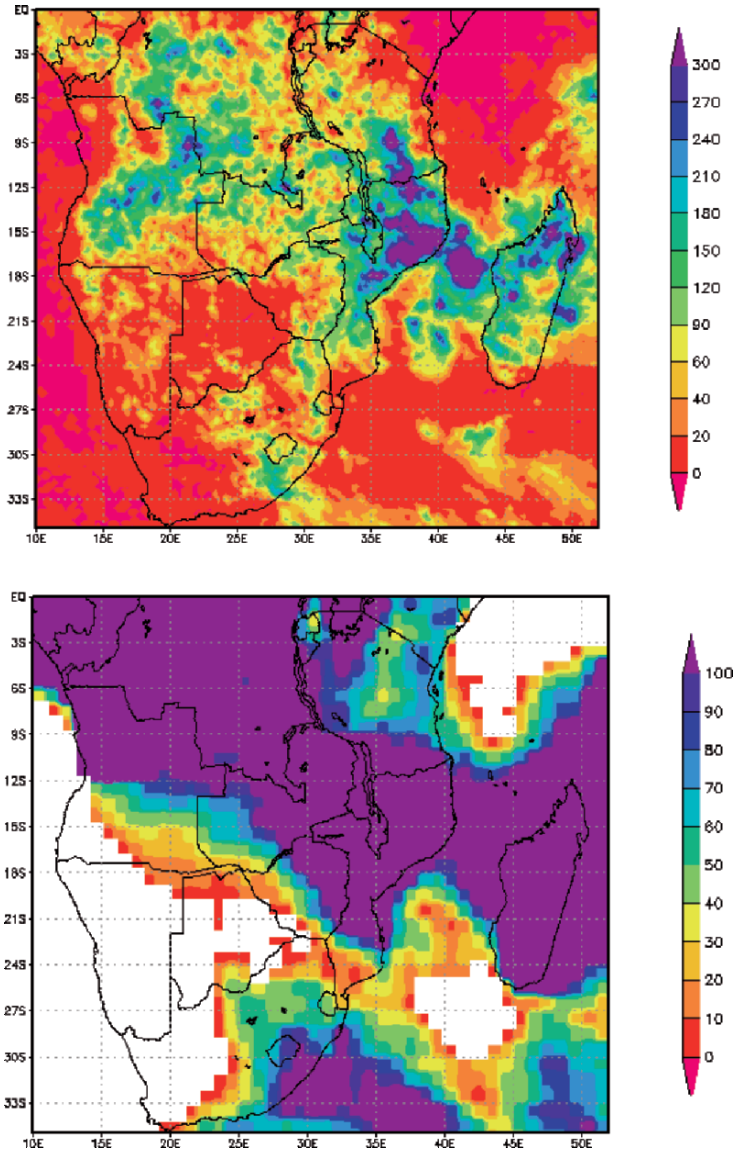
EQ
3S
6S
9S
12S
15S
18S
21S
24S
27S
30S
33S
10E
15E
20E
25E
30E
35E
40E
45E
50E
300
270
240
210
180
150
120
90
60
40
20
0
100
90
80
70
60
50
40
30
20
10
0

Plate 18

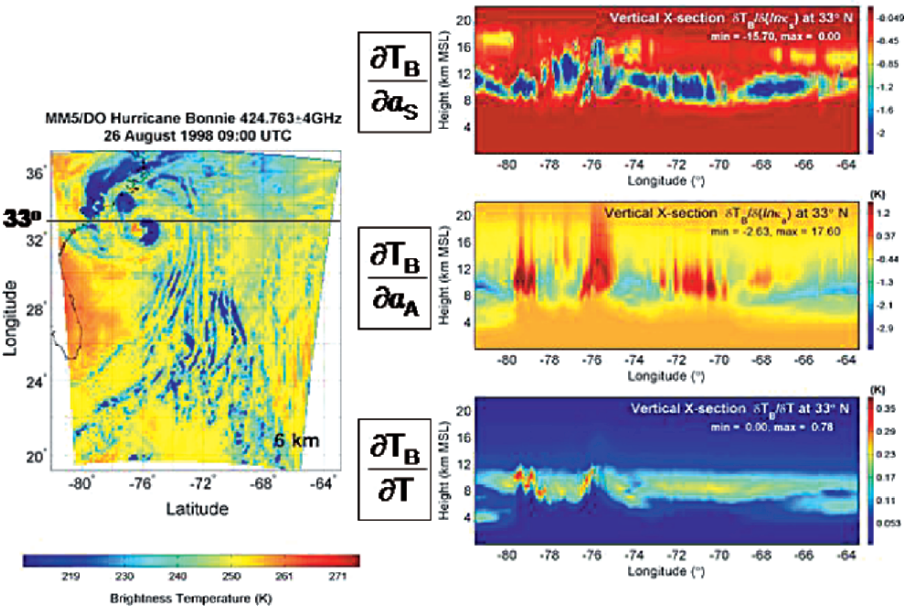

Plate 19

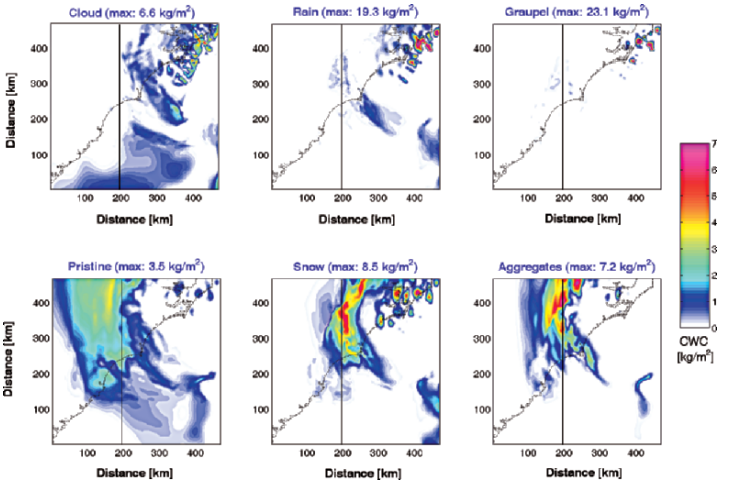

Plate 20a

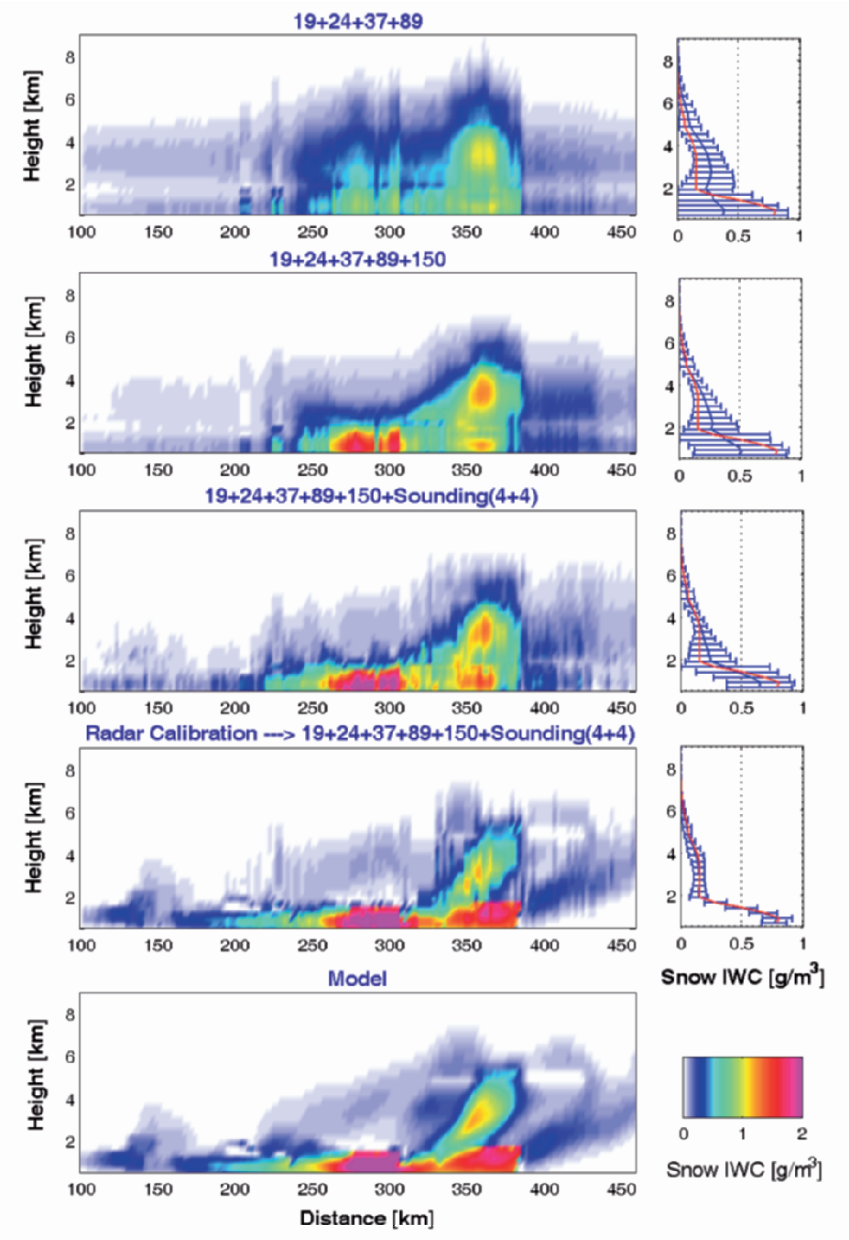
19+24+37+89
19+24+37+89+150
19+24+37+89+150+Sounding(4+4)
Radar Calibration ---> 19+24+37+89+150+Sounding(4+4)
Model
Height [km]
Distance [km]
Snow IWC [g/m3]

Plate 20b

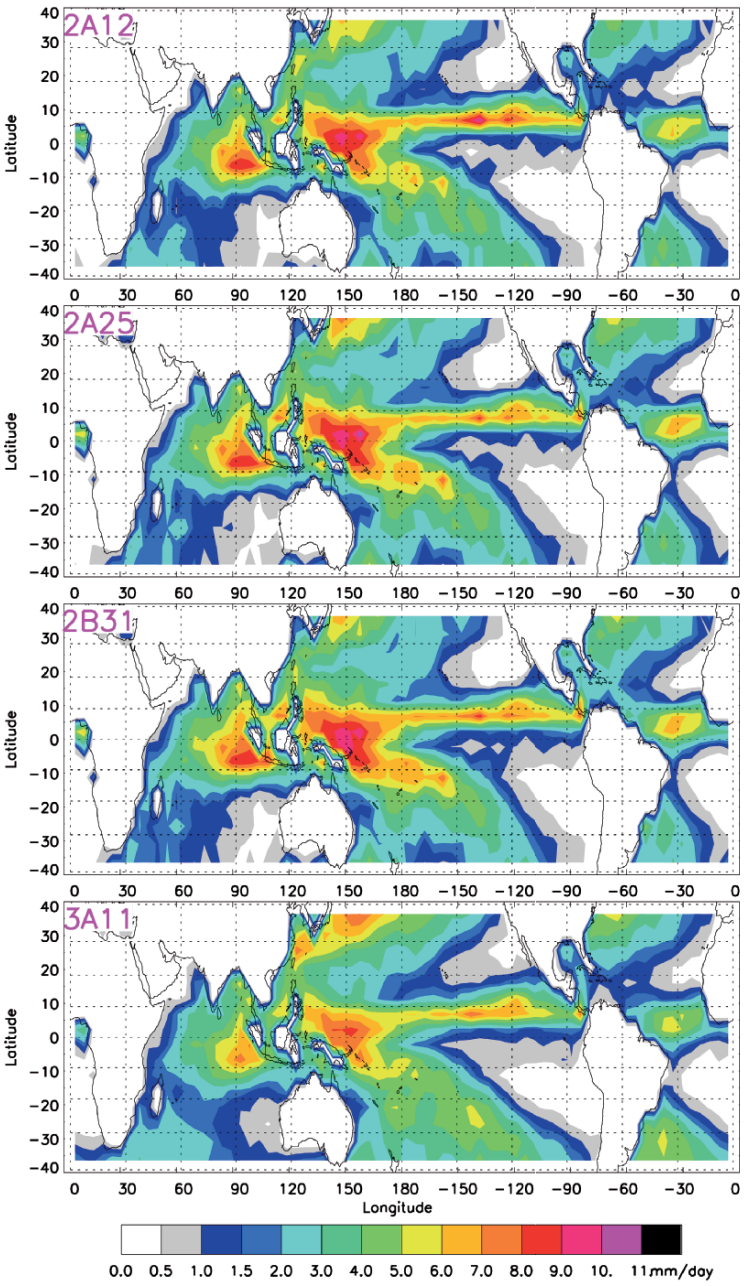
2A12
2A25
2B31
3A11
Latitude
Longitude
40 30 20 10 0 −10 −20 −30 −40
0 30 60 90 120 150 180 −150 −120 −90 −60 −30 0
0.0 0.5 1.0 1.5 2.0 3.0 4.0 5.0 6.0 7.0 8.0 9.0 10. 11mm/day

Plate 21